THE JOURNAL OF PHYSICAL CHEMISTRY C
A JOURNAL OF THE AMERICAN CHEMICAL SOCIETY

Open Access
This article is licensed under CC-BY 4.0

pubs.acs.org/JPCC
Article

Orientation-Dependent Oxygen Evolution Activity of Epitaxial Ruddlesden–Popper $Pr_{0.5}Ca_{1.5}MnO_4$ Thin Films

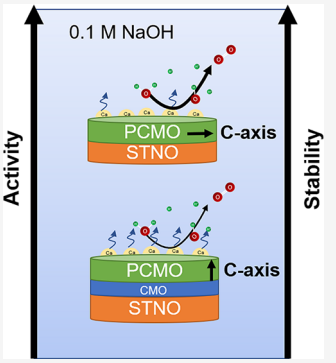
Fatemeh Ebrahimi, Natalie Ottinger, Alexandr Belenchuk, Oleg Shapoval, Christopher Hausmann, Qian Ma, Vasily Moshnyaga, and Christian Jooss*

Cite This: J. Phys. Chem. C 2024, 128, 95–103

Read Online

ACCESS | Metrics & More | Article Recommendations | Supporting Information

ABSTRACT: Studying the oxygen evolution reaction (OER) on anisotropic perovskite oxides with different surface orientations improves our understanding of how surface structure, chemistry, catalytic stability, and activity are related. Here, we present a comparative electrochemical study of (001)- and (010)-oriented epitaxial thin films of Ruddlesden–Popper (n = 1) $Pr_{0.5}Ca_{1.5}MnO_4$ (RP-PCMO) grown on Nb:$SrTiO_3$ (STNO) substrates of different orientations with using buffer layers. The results on epitaxial films are compared with those of the RP-PCMO powder. The OER activity and stability are studied using cyclic voltammetry and rotating ring disk electrodes under alkaline conditions. In addition, an analysis of their surface structure and chemistry by AFM and XPS before and after electrochemical measurements was carried out. The RP-PCMO powder shows high stability during electrochemical cycling. In contrast, the two differently oriented thin films are both corroding, while the (010)-oriented films reveal a higher activity and stability than the (001)-oriented ones. The variation in electrochemical activity and stability of the polycrystalline and single-crystalline RP-PCMO electrodes of different orientations is related to their different surface chemistry. In particular, it depends on the different Mn/Pr/Ca ratios and their different rates of Ca leaching, which is governed by the orientation-dependent Ca hydroxide surface concentration.



Downloaded via 89.149.68.159 on January 28, 2024 at 04:58:38 (UTC).
See https://pubs.acs.org/sharingguidelines for options on how to legitimately share published articles.

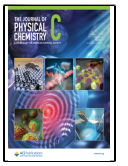
1. INTRODUCTION

Our society's increasing energy demand and the global environmental crisis have stimulated worldwide research activities on new energy conversion and storage systems. It was predicted that electrochemical devices such as fuel cells and rechargeable metal–air batteries can be used for various applications in the future.[1] Oxygen electrocatalysis, including oxygen reduction reaction (ORR) and oxygen evolution reaction (OER), has been extensively studied over the past decades because of its vital role in energy conversion and storage devices.[2] Studies have shown that scaling relationships can be established between the binding energies of intermediate species such as HO*, HOO*, and O* (for the OER) on oxide surfaces.[3,4] The scaling relations suggest that only one free parameter, i.e., the oxygen adsorption energy on a single metal site, determines the free energy diagram and, thereby, the activity. The result is a volcano-shaped relationship between the catalytic activity and calculated oxygen adsorption energy.[3] Even though progress is evident in volcano-like descriptors based on the bulk properties of materials, the mechanisms are still not very well-understood.[5] They depend not only on the intrinsic bulk material properties but also on the surface orientation and surface chemistry.

Highly stable transition metal oxides (TMO) have been widely investigated as electrocatalysts for energy conversion and storage devices.[6,7] Among them, perovskite-type ABO_3 oxides have been extensively considered since many of them exhibit good catalytic activity, stability, and structural flexibility. Various approaches have been utilized to increase the OER or ORR activities of perovskite materials. These strategies include A site doping,[8,9] B site doping,[10] structural adjustments through extension to double perovskites,[11,12] and alterations in covalence.[13] Moreover, the changes in surface chemistry and termination of perovskites have a significant impact on the OER activity.[14,15] For example, OER can be tuned by controlling the as-prepared surface termination of nickelates.[16,5] In particular, comparing epitaxial thin films of different orientations with powders might provide critical new insights into the effects of surfaces,[17] ferroelectric order,[18] and strain[19,20] on the OER.

Manganites represent promising materials for electrocatalytic water oxidation due to the pronounced redox activity of Mn.[21] However, the activity and stability of manganite perovskites depend strongly on their detailed structure and doping.[22,23] Previous studies revealed that the Ruddlesden–Popper type of layered perovskite manganite, i.e., $Pr_{1-x}Ca_{1+x}MnO_4$ at half doping x = 0.5 (RP-PCMO),

Received: September 28, 2023
Revised: December 1, 2023
Accepted: December 11, 2023
Published: December 23, 2023



© 2023 The Authors. Published by American Chemical Society

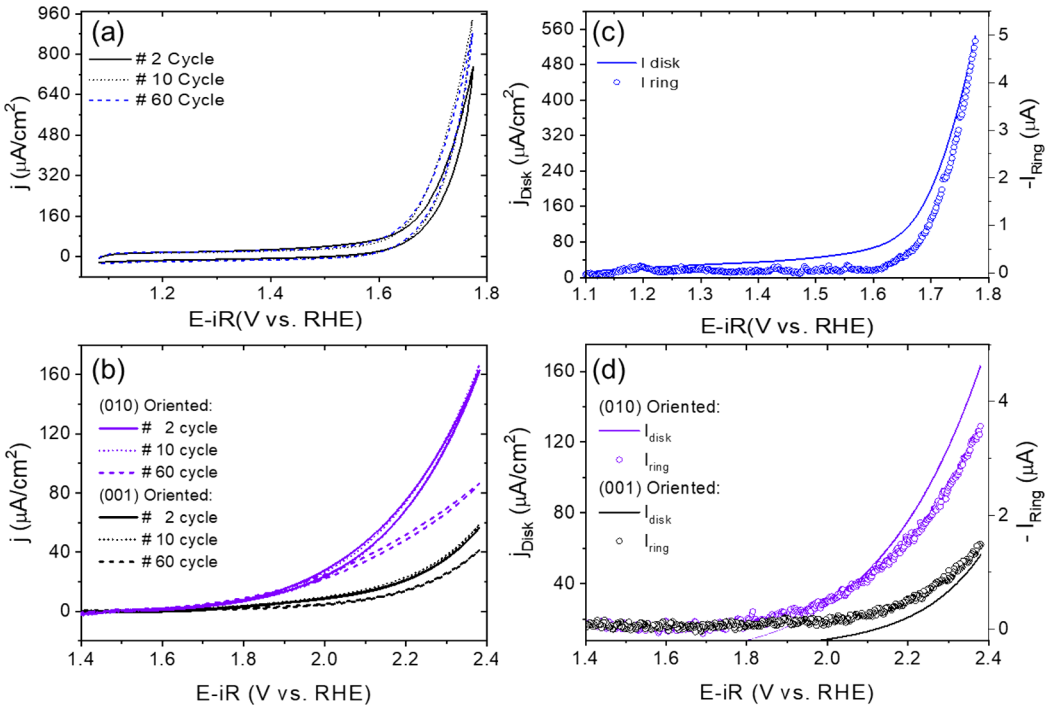


Figure 1. Comparison of oxygen evolution of Ruddlesden−Popper PCMO powder and epitaxial films of different orientations. (a) Second, 10th, and 60th scans of the CV measurements of powders; (b) (010)-oriented and (001)-oriented thin films; (c) RRDE measurements of the powder and (d) of the films. In the RRDE measurements, the corresponding ring currents are depicted as open circles. For all RRDE measurements, the forward direction of the second scan is selected, while the ring potential is 0.4 V vs RHE. All experiments were performed with a 0.1 NaOH argon-purged electrolyte at 20 mV/s and 1600 rpm. Note that the geometrical disk area is used in the calculation of current density j of the powder electrode.

possesses improved stability compared to the three-dimensional $Pr_{1-x}Ca_xMnO_3$ at $x = 0.5$.[21] This was interpreted as due to an improved ability to acquire excess oxygen.[24] Here, by performing a comparative study of the OER activity and stability of RP-PCMO powders and epitaxial films with (010) and (001) orientations, we demonstrate that huge differences in the electrochemical performance are related to different surface chemistry. In particular, using X-ray photoemission spectroscopy (XPS), we observed a pronounced difference in the chemical surface composition of the two films and of the powder that can be correlated to their different initial and later stage of the OER activities.

2. EXPERIMENTAL METHODS

2.1. Powder Preparation. Appropriate ratios of Pr_6O_{11} (CAS 12037-29-5), $CaCO_3$ (CAS 471-34-1), and Mn_2O_3 (CAS 1317-34-6) powders (Sigma-Aldrich) were mixed and thoroughly ground in a planetary ball mill (Retsch). The powder was annealed twice for 12 h at 900 °C and once for 12 h at 1100 °C (Nabertherm, HTCT 01/16), with intermediate grindings. Pellets with a diameter of 2.5 cm were uniaxially cold pressed (Janssen HWP 20) at a pressure of 120 bar for 20 min and sintered for 24 h at 1500 °C. The proof of the phase purity of $Pr_{0.5}Ca_{1.5}MnO_4$ is presented by the XRD pattern in Figure S1. The morphology of the pressed pellet is shown in Figure S2.

2.2. Thin-Film Deposition Technique. Epitaxial thin films were grown by metalorganic aerosol deposition (MAD) based on the pyrolysis of aerosols of metalorganic precursors at the surface of a heated substrate.[17] A mixture of acetylacetonates of Pr, Ca, and Mn (Sigma-Aldrich) dissolved in dimethylformamide with controlled molar ratios of the precursors in the solution was employed for the growth of single-phase RP-PCMO and $CaMnO_3$ (CMO) films by controlling the molar ratios of the precursors in the solution. To obtain the (010)-orientation of RP-PCMO films, commercial (110)-oriented substrates Nb:$SrTiO_3$ (STNO) were used. The (001)-oriented RP-PCMO films were grown on CMO-buffered STNO (100) substrates. The growth at 750 °C with a rate of 0.2 nm/s was established to be optimal for (010)-oriented RP-PCMO films, but the optimized conditions for deposition of (001)-oriented RP-PCMO were entirely different, 920 °C and 0.02 nm/s.

2.3. Thin-Film Structural Characterization. The growth of phase-pure (010)- and (001)-oriented thin films of around 40 nm thickness on STNO (110) and CMO-buffered STNO (001), respectively, was confirmed by X-ray diffraction (XRD) and X-ray reflection (XRR); see Figure S3. The analysis of the crystallographic structure of epitaxial thin films was performed by XRD in the Θ−2Θ Bragg−Brentano geometry using a Bruker D8 Advance diffractometer (Cu $K\alpha$ radiation). The thickness of the films was determined from XRR oscillations by frequency analysis using fast Fourier transformation. The surface morphology was characterized by atomic force microscopy (AFM) using an MFP-3D Classic (Asylum Research) in the tapping mode; see Figure S4.

2.4. Electrochemistry. Electrochemical measurements were carried out by means of a bipotentiostat setup of Interface 1000E potentiostats (Gamry Instruments, Inc., Warminster, PA, USA), and a rotating ring disk electrode (RRDE)-3A rotator (ALS Co., Ltd., Tokyo, Japan) was used to perform electrochemical measurements. For the powder experiments, we used a glassy carbon (GC) electrode (4 mm

https://doi.org/10.1021/acs.jpcc.3c06472
J. Phys. Chem. C 2024, 128, 95−103

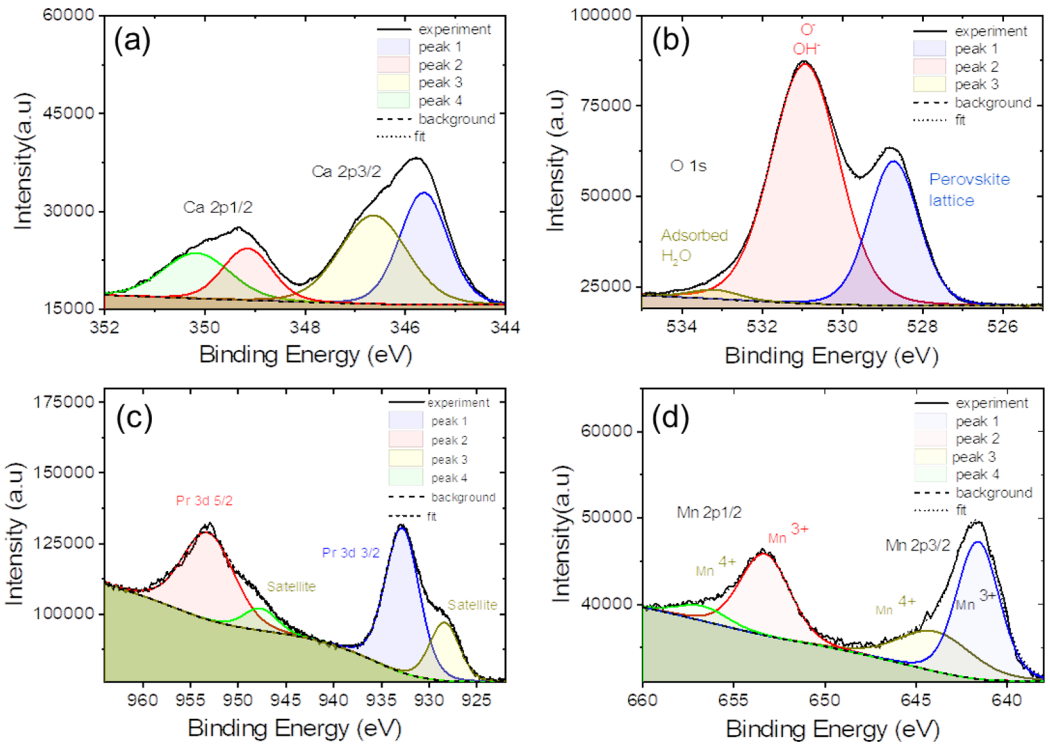


Figure 2. XPS core-level spectra of (a) Ca 2p, (b) O 1s, (c) Pr 3d, and (d) Mn 2p for the pristine RP-PCMO powders, together with fitted Lorentzian peaks.

diameter). The electrode was polished to a mirror finish with a diamond slurry (3 μm) and alumina slurry (1 and 0.3 μm). Catalyst inks were prepared to a 5 mg/mL catalyst concentration with the solvent tetrahydrofuran (THF) and 1 mg/mL carbon black, a conductive additive. For preparing the catalyst layer, the ink of each sample (5 μL) was cast on the surface of the GC electrode and left to dry in air. The PCMO| STNO thin-film electrodes were prepared for the RRDE disk electrode with a diameter of 4 mm and a Pt ring electrode with an inner diameter of 5 mm and an outer diameter of 7 mm. All electrochemical reactions were performed in a 0.1 M NaOH electrolyte. The electrolyte solution was prepared by diluting NaOH solution (Sigma-Aldrich, Munich, Germany) with deionized water (Milli-Q, >16.5 MΩ). The electrolyte was saturated with Ar gas for at least 30 min before measurements and continuously purged with Ar during the measurements. All potentials were referenced to the reversible hydrogen electrode (RHE) scale.

2.5. XPS. A Kratos AXIS Supra, SPECS PHOIBOS 100 hemispherical XPS analyzer with a monochromatic X-ray source (SPECS FOCUS 500 monochromator, Al Kα radiation, 1486.74 eV) was applied to determine the elemental composition of the powders as well as of the thin films. The pass energy was set to 30 eV with a step size of 0.5 eV for survey and 10 eV with a step size of 0.05 eV for fine spectra. All scans were performed using large-area spectroscopy in the hybrid lens mode with the collimation mode slot. The binding energy scale was corrected by shifting the C 1s main peak energy to 284.9 eV with the charge neutralizer. CasaXPS software was used to calculate the atomic percentages of core levels. The error was given by the standard deviation of the Lorentzian fit and data from the detailed scans of the analyzed lines. The relative sensitivity factors (RSFs) were obtained from the CasaXPS-Supra-Al library. For all elements, except Mn 2p, a Shirley background was used. A Tougaard background was selected for the Mn 2p component. All the XPS investigations of the powders and the thin films were performed on the prepared electrode before and after 10 and 60 cycles of cyclic voltammetry.

3. RESULTS AND DISCUSSION

3.1. Electrochemical Activity and Stability. The OER activity of the RP-PCMO thin films and powder electrodes was characterized using cyclic voltammetry (CV) and rotating ring disk electrodes (RRDE) in Ar-saturated 0.1 M NaOH solution. Figure 1a,b shows the selected CV measurements of the powder as well as the CV of the two differently oriented thin-film electrodes. Due to the large difference of the surface area of powder and films, the onset potential and current densities for OER cannot be compared since we use the geometrical disk surface for the powder electrode. We observe that the current density of the (010)-oriented film is more than 100% higher than that of the (001)-oriented film.

Remarkably, the activity of the powders increased slightly during the first 10 cycles. After 60 cycles, only a slight drop of ~5% at 1.75 V vs RHE) was observed. This indicates a reasonable stability and is in line with the previous study on RP-PCMO powders with different levels of Ca doping.[21] The stability of the differently oriented films was found to vary significantly. Whereas the (010)-oriented film shows a slight increase in a current of 6% from the 10th to 60th cycle at 1.75 V, at a higher potential of 2.2 V, the current, instead, drops by 30%. In contrast, the (001)-oriented film shows a decrease in current from the 10th cycle to the 60th cycle over the entire OER potential range. For example, at 2.2 V, the current drops by 40%. These findings reveal the higher activity and stability of the (010)-oriented RP-PCMO film.

https://doi.org/10.1021/acs.jpcc.3c06472
J. Phys. Chem. C 2024, 128, 95−103

Table 1. Atomic Concentrations of the Close-to-Surface Species of the Pressed Powder Electrode in Atom Percent Obtained from XPS Detailed Scans[a]

powder electrode	Pr 3d	Mn 2p	Mn valence	Ca 2p	Ca(L)	$Ca(OH)_2$	O 1s	(Ca+Pr)/Mn	Ca/Pr
nominal	7.1	14.3	3.5	21.4	21.4	0	57.1	2	3
pristine	13.3	9.8	3.5	7.9	6.0	1.8	69.0	2.2	0.6
10 cycles	14.5	8.1	3.3	8.2	6.7	1.6	69.1	2.8	0.6
60 cycles	5.3	11.9	3.2	6.8	5.2	1.5	76.0	1.0	1.3

[a]The error, as obtained from the standard deviation accounts for ±0.5%. Nominal concentrations represent the bulk values.

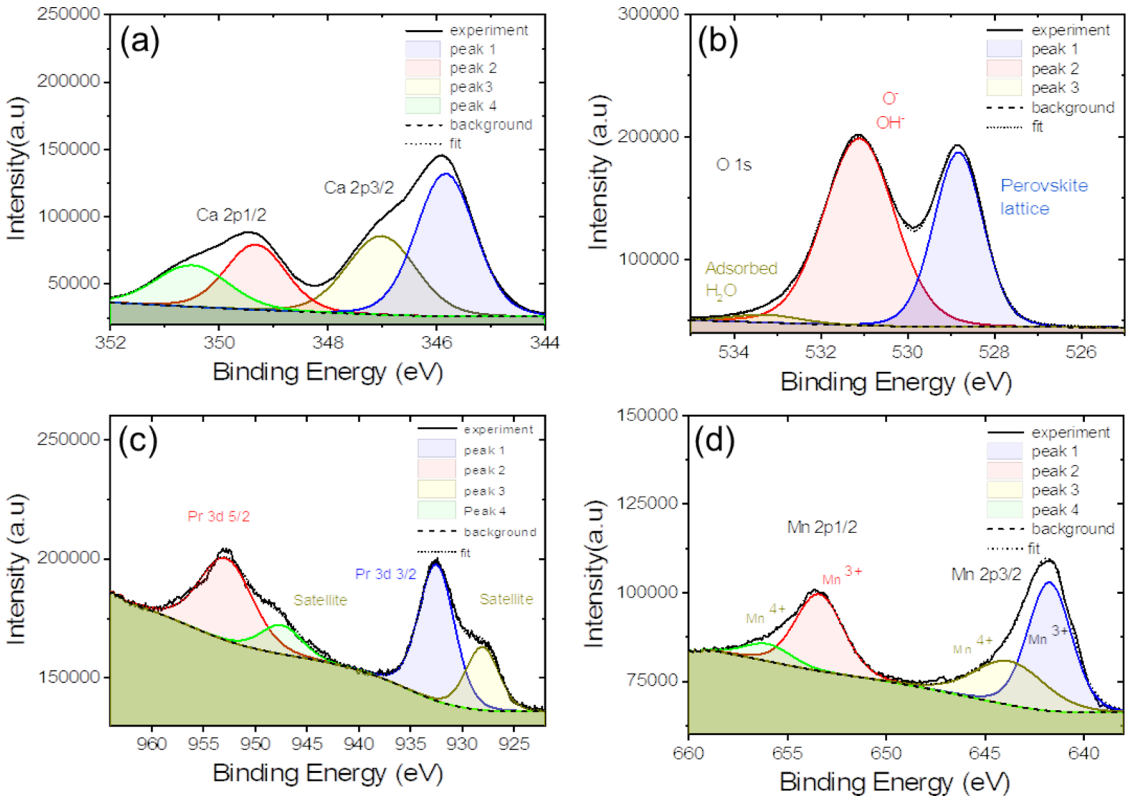


Figure 3. XPS core-level spectra of a pristine (010)-oriented RP_PCMO film; (a) Ca 2p; peaks 1 and 2 represent the lattice perovskite structure, and peaks 3 and 4 correspond to the formation of surface $Ca(OH)_2$ and/or CaO; (b) O 1s, (c) Pr 3d, and (d) Mn 2p. The fitted Gaussian peaks are shown as color-filled curves.

The RRDE setup was employed to verify the OER activity by using a platinum ring electrode for the detection of the oxygen produced by the specimen. Therefore, a potential of 0.4 V vs RHE was applied to the Pt ring electrode, which is sufficient to drive the oxygen reduction reaction (ORR). Under these experimental conditions, the produced oxygen is reduced at the ring electrode under mass-limiting conditions, so that the ring current depends only on the concentration of oxygen.[25] The coincidence of the onset of exponentially rising currents on the disk and ring electrodes for all samples in Figure 1c,d verifies that they originate from the OER. Also, the RRDE measurements confirmed a higher activity of the (010)-oriented film compared to that of the (001)-oriented film. Similar Tafel slopes of around 0.4 V/decade for ring and disk currents (see Figure S5) suggest that the reaction mechanism is the same for both film orientations, and undesired side reactions cannot explain the different disk current densities.

3.2. X-ray Photoelectron Spectroscopy. The technique of X-ray photoelectron spectroscopy (XPS) was employed to investigate RP-PCMO powders and films with different orientations in their pristine state and after electrochemical cycling. With an energy-dependent escape depth of photoelectrons of 5−10 nm, it allows the determination of the close-to-surface chemical composition of all electrodes. This was carefully carried out in the pristine state after 10 and 60 cycles (see the experimental section), including the chemical bonding-induced shifts and oxidation states of the elements.

3.2.1. Ruddlesden−Popper PCMO Powder. In Figure 2, XPS analysis of the pristine RP-PCMO powders is presented via detailed scans. Survey scans of the pressed electrode and pure powder are shown in Figures S6 and S7, respectively. Figure 2a shows the Ca 2p states that are split into $2p_{1/2}$ and $2p_{3/2}$ states at binding energies of approximately 350 and 346 eV, respectively, due to spin−orbit interaction. Each of the two peaks is fitted with two subpeaks. While peak 1 and peak 2 at 345.6 and 349.2 eV, respectively, represent the Ca site in the lattice perovskite structure, the peak 3 and peak 4 at 346.7 and 350.2 eV, respectively, correspond to the formation of $Ca(OH)_2$ and/or CaO species at the surface.[26] In the following, we denote these peaks as lattice Ca(L) and $Ca(OH)_2$ peaks, respectively.

https://doi.org/10.1021/acs.jpcc.3c06472
J. Phys. Chem. C 2024, 128, 95−103

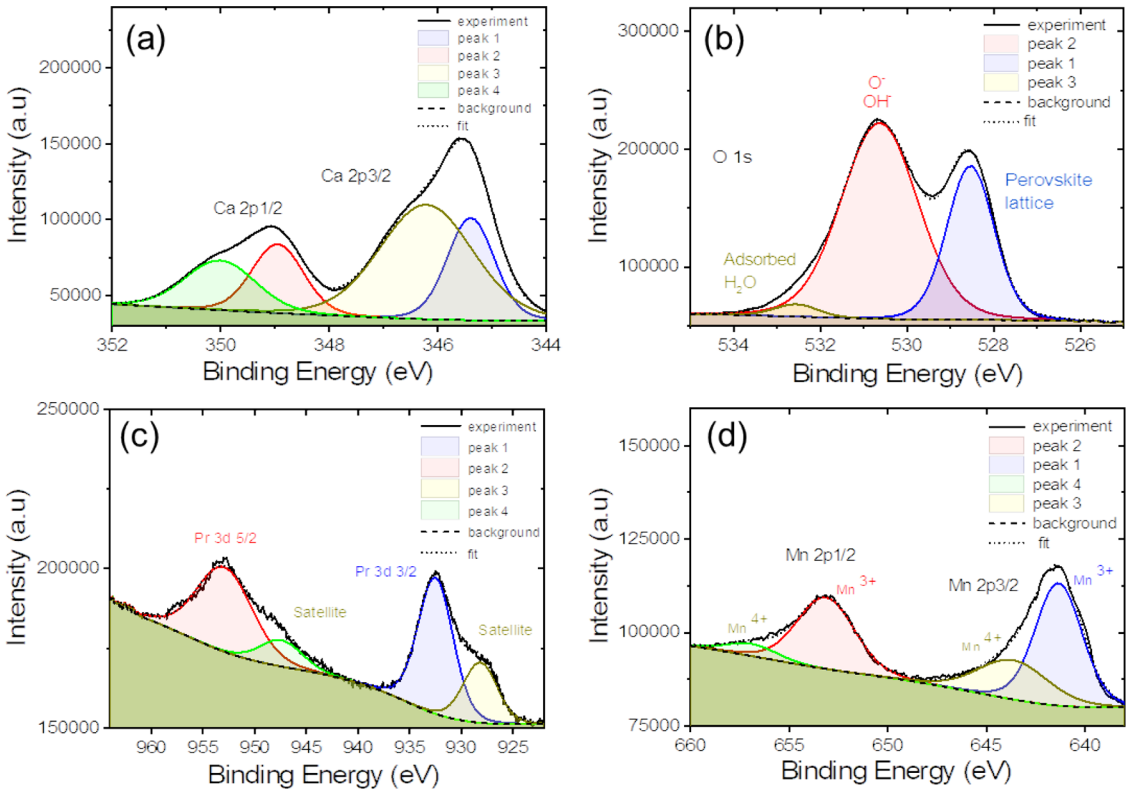


Figure 4. XPS core-level spectra of a pristine (001)-oriented RP_PCMO film; (a) Ca 2p; peaks 1 and 2 represent the lattice perovskite structure, and peaks 3 and 4 correspond to the formation of surface Ca $(OH)_2$ and/or CaO; (b) O 1s, (c) Pr 3d, and (d) Mn 2p. The fitted Gaussian peaks are shown as color-filled curves.

In Figure 2b, the O 1s spectra of the oxides consist of two prominent peaks separated by around 3 eV and an additional small peak at 533.2 eV. The O^{2-} species at the perovskite lattice sites appears at a binding energy of 528.9 eV. Furthermore, various weakly bound O^- and OH^- surface species are visible at 530.97 eV. The O 1s peak 3 represents adsorbed H_2O molecules.[27,28]

Pr species can be measured using the Pr 3d states, which are split into Pr $3d_{3/2}$ and Pr $3d_{5/2}$ levels due to spin−orbit coupling, as visible in Figure 2c. Pr $3d_{5/2}$ is found to be roughly at 932.9 eV, and the energy separation between the Pr $3d_{3/2}$ and Pr $3d_{5/2}$ transitions is around 20 eV with a 3:2 intensity ratio. A strong shoulder can be seen on the lower sides of the Pr $3d_{5/2}$ and Pr $3d_{3/2}$ peaks, corresponding to the so-called shake-down satellite,[15] a collective response of the outer electron cloud to the formation of core holes. These satellites are excluded from the calculation of the Pr atomic percentage.

The Mn 2p core-level spectra, together with their fitting lines, are depicted in Figure 2d. The Mn 2p peak is split owing to spin−orbit coupling and shows an 11.2 eV energy separation that is typical for oxides. Each of the $2p_{1/2}$ and $2p_{3/2}$ states consists of substates, which can be formally attributed to different valence states, i.e., Mn^{3+} (peaks 1 and 2) and Mn^{4+} (peaks 3 and 4).[8]

Table 1 shows the atomic concentrations of the close-to-surface species of the pristine as well as of the cycled powder electrodes; see Figures S8 and S9 for data on cycled powder. Despite the high phase purity confirmed by XRD in Figure S1, the surface concentration of the species strongly deviates from the nominal bulk values. The pristine as well as the cycled stages show Pr-rich and Mn-rich, respectively, Ca-depleted surfaces. During long-term electrochemical cycling, the surface concentration of Mn increases, whereas that of Pr decreases. This might explain the measured drop in the Mn valence state, which is given by the average Mn valence. Furthermore, cycling is accompanied by an increase in close-to-surface oxygen, which cannot be explained by a surface hydroxide since the $Ca(OH)_2$ concentration is small and decreases during cycling. The drop in the (Ca+Pr)/Mn ratio from slightly above 2 to 1 after 60 cycles indicates a possible formation of a MnO_x-rich surface phase.

The strong drop of the surface Pr concentration and the formation of a Mn-rich surface phase are in contrast to the 3D perovskite $Pr_{1-x}Ca_xMnO_3$ with x = 0.3−0.5, where oxygen vacancy-induced Mn reduction and leaching are related to the formation of a PrO_x-rich surface phase;[23] see also Supporting Information in ref 29. The formation of a PrO_x-rich surface results in fast deactivation and corrosion of the 3D PCMO. In contrast, our results indicate that the RP-PCMO powder may act as a seed for the formation of a rather stable and catalytically active MnO_x-rich surface, which would explain the high stability of the powder.

3.2.2. Ruddlesden−Popper PCMO Epitaxial Films. Similar analysis was performed by using X-ray photoelectron core-level spectroscopy of the two differently oriented RP-PCMO films. Detailed scans for the pristine films are shown in Figures 3 and 4. For wide scans, see Figures S10 and S11. A closer look at the Ca peaks of both films shows the contribution of surficial $Ca(OH)_2$ or CaO, which was also observed in the case of powders. Moreover, Figures 3a and 4a show that the ratio of Ca in hydroxide to that in the perovskite lattice is higher in the (001)-oriented (less active) film than in the (010)-oriented

https://doi.org/10.1021/acs.jpcc.3c06472
J. Phys. Chem. C 2024, 128, 95−103

Table 2. Close-to-Surface Concentration of the Species in Atom Percent of (010)-Oriented Films Based on XPS Analysis[a]

(010) film	Pr 3d	Mn 2p	Mn valence	Ca 2p	Ca(L)	$Ca(OH)_2$	O 1s	(Ca+Pr)/Mn	Ca/Pr
nominal	7.1	14.3	3.5	21.4	21.4	0	57.1	2	3
pristine	7.0	7.4	3.2	17.8	9.3	6.2	67.9	3.4	2.6
10 cycles	11.9	4.7	3.3	8.4	2.9	5.5	74.9	4.3	0.7
60 cycles	18.5	6.3	3.2	4.5	1.6	2.8	70.8	3.7	0.2

[a]The error, as obtained from the standard deviation, accounts to ±0.5%. Nominal concentrations represent the bulk values.

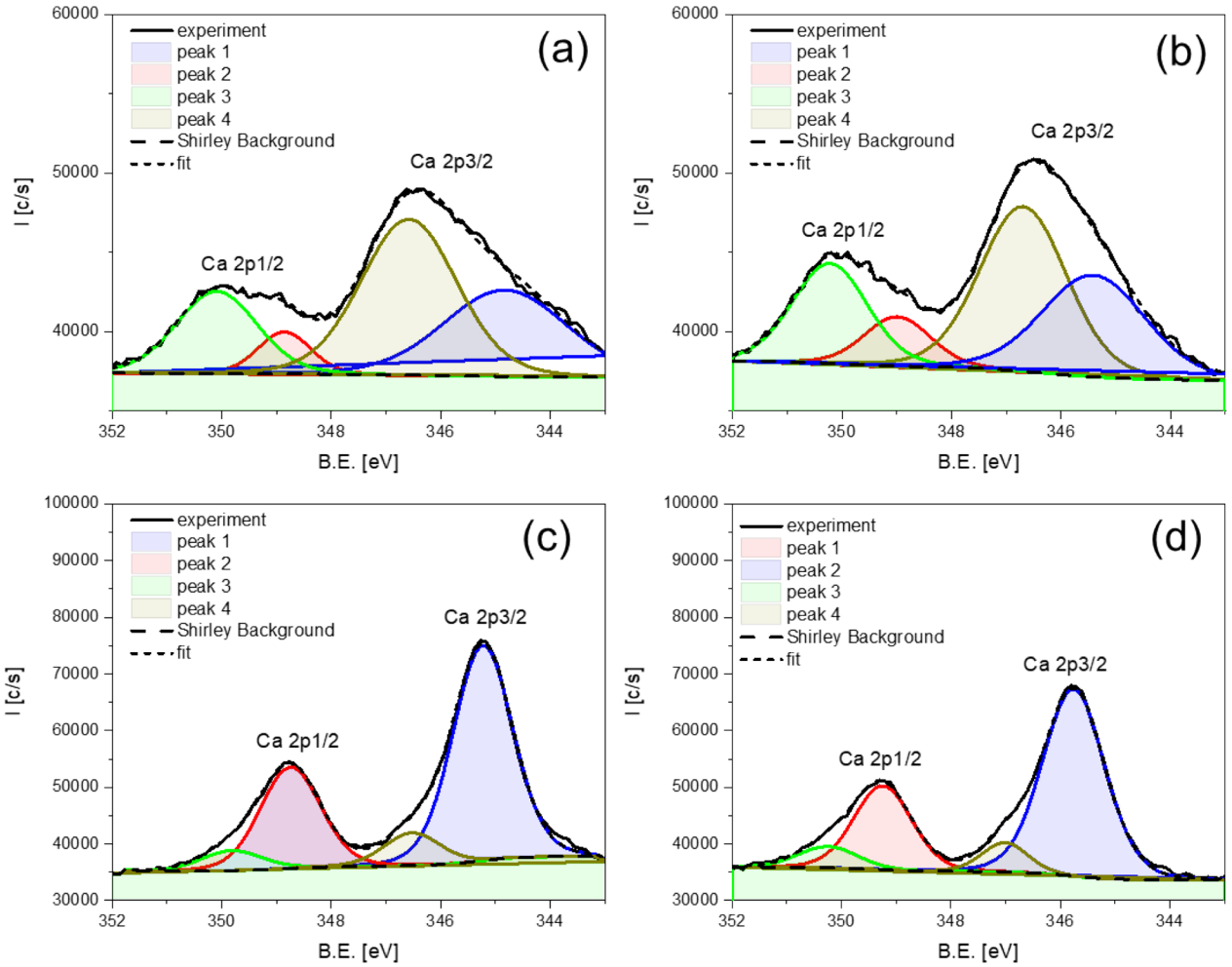


Figure 5. XPS core-level spectra of the Ca 2p (a) (010)-oriented film after 10 CV and (b) (010)-oriented film after 60 CV and (c) (001)-oriented film after 10 CV and (d) (001)-oriented film after 60 CV. The fitted Lorentzian peaks are shown as color-filled curves.

film. We denote these peaks as lattice Ca(L) and $Ca(OH)_2$ peaks, respectively.

As for the O 1s core level, the contributions of OH and adsorbed H_2O at the surface of both (010)- and (001)-oriented films can be seen in Figures 3b and 4b. It is observed that the contribution of OH in the O 1s peak is more pronounced for the less active (001)-oriented film.

Tables 2 and 3 list the determined values of close-to-surface concentrations of all species for the two differently oriented films in the pristine and electrochemically cycled states. The values are based on fits of the data in the XPS detailed scans in Figures 3 and 4, as well as Figures S12 and S13 and Tables S1−S3.

In the pristine states, both films show Ca- and Mn-depleted surfaces compared to the nominal bulk values. Pr is close to the expected values, whereas O seems to be enriched. We attribute this to the absorbed water/hydroxide layer. This is supported by the presence of a significant $Ca(OH)_2$ contribution of 6.2 at. % for the (010) and 10.0 at. % for the (001) films in the pristine state. In the O 1s spectra (Figure S13), a large amount of OH species is observed, which is quantified in Table S1. This indicates hydroxide concentrations close to the surface of about 23 and 27 at. % for the (001) and (010) films, respectively.

Upon electrochemical cycling, both films exhibit the formation of a Pr-rich surface, whereas Ca depletes, and Mn remains stable. This trend is more pronounced for (010) than for (001) films. While the close-to-surface Ca concentration decreases, the enrichment of Pr gives rise to a rather high and rather stable (Ca+Pr)/Mn ratio above the nominal bulk value of 2. The drop of the Mn valence state upon cycling for both films seems to be in contradiction to the increase of the O. After subtraction of the OH contribution in Table S1, we find that for the (001), O(L) drops after 10 cycles and recovers to

https://doi.org/10.1021/acs.jpcc.3c06472
J. Phys. Chem. C 2024, 128, 95−103

the original values after 60 cycles. In contrast, for the (010) film, O(L) increases during cycling, possibly indicating the formation of a PrO_x-rich phase similar to the 3D PCMO films.

AFM investigation of the surfaces before and after 60 cycles in NaOH did not show significant changes in the morphology (Figure S4). This indicates that the change in composition only affects the surface layer and is not related to the more severe dissolution of the electrode material during cycling. The slightly increased surface roughness of the (001)-oriented film compared to that of the (010)-oriented film as a result of the preparation process is preserved during cycling.

In the following, we provide a closer look at the evolution of the Ca species for both film orientations upon cycling; see Figure 5. The strong decrease in the surface Ca concentration of both films during CV cycling is related to the pronounced relative changes in the Ca hydroxide/oxide and Ca perovskite lattice peaks. Remarkably, the (010)-oriented film reveals an increase in the ratio of Ca hydroxide to the Ca lattice site after 10 cycles compared to the pristine state. This ratio did not change further after additional cycles. In contrast, the (001)-oriented film exhibits a strong drop in the Ca hydroxide to Ca lattice site ratio after 10 cycles and continued after 60 cycles. In contrast to the pristine state of the (001) film, where the surface is dominated by Ca hydroxide, the surface is dominated by the Ca lattice site species after electrochemical cycling. These findings suggest a different chemical stability of Ca hydroxide on the two different surfaces. For the (010) film, the remaining Ca surface concentration after 60 cycles seems to consist of approximately 63% of the $Ca(OH)_2$ species and only approximately 37% of the Ca(L) species.

In contrast, for the (001)-oriented film, where the drop in the overall Ca concentration after 60 cycles is less severe, the Ca(L) perovskite lattice species becomes dominant at the surface. The surface concentration of Mn as well as its valence, which is formally ascribed as a Mn^{3+} and Mn^{4+} mixture, did not show considerable changes upon electrochemical cycling; see also Figure S12.

3.3. Discussion. Electrochemical investigation combined with XPS studies of the close-to-surface concentration of Pr, Mn, Ca, and O species reveals a huge difference between the surface chemistry of RP-PCMO powder and epitaxial thin films of initially the same bulk phase, as summarized in Figure 6. Cyclic voltammetry confirms the reasonable activity and high stability of the powder electrode of RP-perovskite under alkaline conditions, which has been also reported in previous investigations.[21] This is in line with the observation that the XPS spectra of powder electrode samples only showed a reduction of the Pr concentration, whereas Ca is stable and Mn is even increased after 60 cycles. Since the (Ca+Pr)/Mn ratio decreases from 2 to 1 after 60 electrochemical cycles, we suggest that the RP-PCMO powder surface transforms into a MnO_x-rich surface phase that is located on top of a rather stable perovskite seed.

In contrast to the powder, both thin-film orientations show a rapid drop of activity. Simultaneously, the activity and stability during electrochemical cycling of the (010)-oriented film are higher than those of the (001)-oriented one. For the OER of the epitaxial films, the most relevant observation is that the initial A to B site ratio (Ca+Pr)/Mn is >3, which is much higher than the stoichiometric value of 2. As visible in Figure 6b,c, the rather low Mn surface concentration remains more or less stable, but the surface deactivates via the formation of a

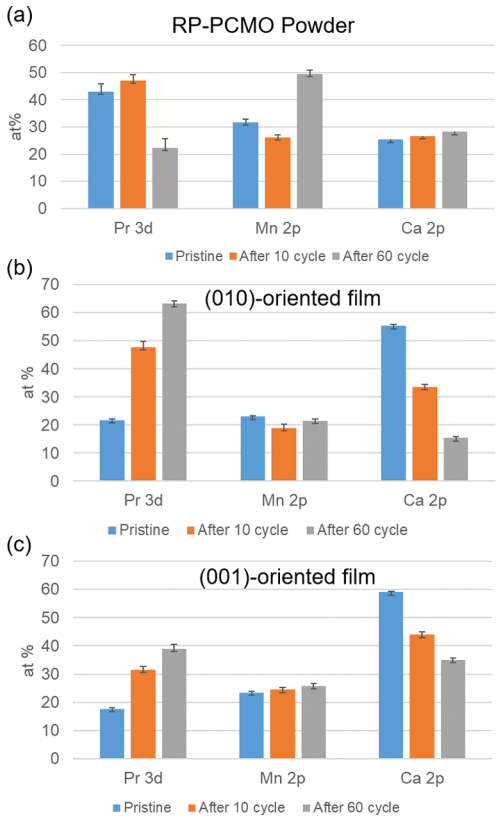


Figure 6. Atomic percentages of close-to-surface cations obtained from Tables 1−3. The changes upon electrochemical cycling are visible. Pressed powder electrodes (a), (010) (b), and (001) films (c). Normalization takes into account the cationic species only.

PrO_x-rich surface, very similar to (001)-oriented 3D PCMO thin films at the same level of doping.

Interestingly, the close-to-surface concentrations of the less active (001) film and the more highly active (010) film are similar in the pristine state. Only, the (001) film, in its pristine state, shows a higher $Ca(OH)_2$ to Ca(L) ratio and approximately 1% less Mn. Consequently, the different surface chemistry in the initial state can only explain why the current density of the (010)-oriented film is more than 100% higher than that of the (001)-oriented film if $Ca(OH)_2$ plays an important role. Indeed, the role of Ca hydroxide species in the stabilization of active Mn^{3+} states was discussed for another layered manganese oxide compound, namely, Ca birnessite.[30] However, the valence states of Mn in both epitaxial orientations are 3.2 (010) and 3.3 (001), respectively, which are very similar and do not connect to the higher hydroxide surface concentration at the (010) films.

The strong increase in Pr and drop in Ca species at the surface during electrochemical cycling are the most prominent differences between the films and the powder.

As discussed above, the formation of a Pr-rich surface is known to be the main degradation mechanism of the (001)-surface of the three-dimensional $Pr_{0.67}Ca_{0.33}MnO_3$ system. In this system, it is due to a rapid leaching of both Mn (due to Mn^{2+} formation) and Ca at the surface.[23] In contrast, Mn reduction and leaching are not observed in the present study since both the valence and close-to-the-surface concentration remain stable. The reduction of Mn due to oxygen vacancy formation, which has been reported for the three-dimensional

https://doi.org/10.1021/acs.jpcc.3c06472
J. Phys. Chem. C 2024, 128, 95−103

Table 3. Close-to-Surface Concentration of the Species in Atom Percent of (001)-Oriented Films Based on the XPS Analysis[a]

(001) film	Pr 3d	Mn 2p	Mn valence	Ca 2p	Ca(L)	$Ca(OH)_2$	O 1s	(Ca+Pr)/Mn	Ca/Pr
nominal	7.1	14.3	3.5	21.4	21.4	0	57.14	2	3
pristine	5.0	6.6	3.3	16.8	6.8	10.0	71.6	3.3	3.3
10 cycles	9.5	7.4	3.3	13.3	11.3	1.9	69.9	3.0	1.4
60 cycles	11.1	7.4	3.3	10.0	8.5	1.5	71.5	2.9	0.9

[a]The error, as obtained from the standard deviation, accounts to ±0.5%. Nominal concentrations represent the bulk values.

PCMO, is thus absent in RP-PCMO films, and deactivation mainly occurs via the loss of surface Ca.

The higher stability of the RP-PCMO powder compared to the differently oriented RP-PCMO films is thus correlated to the different $Ca(OH)_2$ concentrations in the pristine state: Whereas it is 1.8 atom % for the powder (Table 1), it amounts to 6.2 and 10.0 atom % in the (010)- and (001)-oriented films, respectively (Tables 2 and 3). Indeed, the reduction of the $(Ca(OH)_2)$ concentration seems a major channel for the loss of surface Ca, which aligns with existing literature, reporting the high solubility of calcium hydroxide in sodium hydroxide (NaOH) electrolytes in a low molar concentration range up to 3.5 M.[31] Consequently, the solubility of $Ca(OH)_2$ is a crucial factor governing the concentration of calcium ions on the surfaces of the RP-PCMO thin films. The findings further emphasize the importance of considering the impact of electrolyte-specific effects on the orientation-dependent surface chemistry of electrode materials.

4. CONCLUSIONS

$Pr_{0.5}Ca_{1.5}MnO_4$ powder and thin films with two different orientations were studied concerning electrocatalytic oxygen evolution. Our results confirm that anisotropy is entangled with different surface orientations that affect the evolution of the surface chemistry. The (001)-oriented films shows lower activity than the (010)-oriented films, while in both films, the onset of OER is shifted to a slightly higher potential than that in the powder electrode. The Mn valence, approximated as a mixture of Mn^{3+} and Mn^{4+} species, is observed as unchanged upon cyclic voltammetry. It is revealed that there is a contribution of Ca oxide/hydroxide on the surface of films, which is more pronounced at the surface of the (001)-oriented film in the pristine state and evolves as the dominant Ca species at the surface of the (010) film during electrochemical cycling. In contrast to 3D PCMO, the reduction of Mn due to oxygen vacancy formation is suppressed in the RP-PCMO films.

■ ASSOCIATED CONTENT

Supporting Information

The Supporting Information is available free of charge at https://pubs.acs.org/doi/10.1021/acs.jpcc.3c06472.

Synthesis details and characterization of RP-$Pr_{0.5}Ca_{1.5}MnO_4$ powder; XRD and SEM analysis of the synthesized powder; XRD and XRR characterization of the (010)- and (001)-oriented RP-PCMO films; AFM images showing film surfaces before and after electrochemistry; Tafel plots and electrochemical measurements for RP-PCMO powders and thin films; XPS analysis of RP-PCMO powder and film electrodes, including Ca 2p and Mn 3d detailed scans; evolution of Mn 2p and O 1s core-level spectra in films before and after electrochemistry (PDF)

■ AUTHOR INFORMATION

Corresponding Author

Christian Jooss − *Institute of Materials Physics, University of Goettingen, Göttingen 37077, Germany;* orcid.org/0000-0002-8762-9359; Email: cjooss@gwdg.de

Authors

Fatemeh Ebrahimi − *Institute of Materials Physics, University of Goettingen, Göttingen 37077, Germany;* orcid.org/0000-0002-2532-5691

Natalie Ottinger − *Institute of Materials Physics, University of Goettingen, Göttingen 37077, Germany;* orcid.org/0000-0001-8237-3406

Alexandr Belenchuk − *Physics of Semiconductors & Devices Laboratory, Moldova State University, Chişinău MD-2009, Moldova*

Oleg Shapoval − *Physics of Semiconductors & Devices Laboratory, Moldova State University, Chişinău MD-2009, Moldova*

Christopher Hausmann − *Institute of Materials Physics, University of Goettingen, Göttingen 37077, Germany*

Qian Ma − *Institute of Materials Physics, University of Goettingen, Göttingen 37077, Germany*

Vasily Moshnyaga − *First Physical Institute, University of Goettingen, Goettingen 37077, Germany*

Complete contact information is available at: https://pubs.acs.org/10.1021/acs.jpcc.3c06472

Notes

The authors declare no competing financial interest.

■ ACKNOWLEDGMENTS

Financial support from the DFG via the CRC 1073, in particular in projects C01 and Z02, is gratefully acknowledged.

■ REFERENCES

(1) Caramia, V.; Bozzini, B. Materials science aspects of zinc-air batteries: A review. *Mater. Renewable Sustainable Energy* **2014**, *3*, 1−12.

(2) Seh, Z. W.; Kibsgaard, J.; Dickens, C. F.; Chorkendorff, I.; Nørskov, J. K.; Jaramillo, T. F. Combining theory and experiment in electrocatalysis: Insights into materials design. *Science* **2017**, *355*, No. eaad4998.

(3) Man, I. C.; Su, H.; Calle-Vallejo, F.; Hansen, H. A.; Martínez, J. I.; Inoglu, N. G.; Kitchin, J.; Jaramillo, T. F.; Nørskov, J. K.; Rossmei, J. Universality in Oxygen Evolution Electrocatalysis on Oxide Surfaces. *ChemCatChem* **2011**, *3*, 1159−1165.

(4) Rossmeisl, J.; Qu, Z.-W.; Zhu, H.; Kroes, G. J.; Nørskov, J. K. Electrolysis of water on oxide surfaces. *J. Electroanal. Chem.* **2007**, *607*, 83−89.

(5) Liang, Q.; Brocks, G.; Bieberle-Hütter, A. Oxygen evolution reaction (OER) mechanism under alkaline and acidic conditions. *Journal of Physics: Energy* **2021**, *3*, No. 026001.

(6) Yuan, C.; Wu, H. B.; Xie, Y.; Lou, X. W. Mixed transition-metal oxides: Design, synthesis, and energy-related applications. *Angewandte Chemie - International Edition* **2014**, *53*, 1488−1504.
(7) Sun, C.; Alonso, J. A.; Bian, J. Recent Advances in Perovskite-Type Oxides for Energy Conversion and Storage Applications. *Adv. Energy Mater.* **2021**, *11*, No. 2000459.
(8) Xu, X.; Chen, Y.; Zhou, W.; Zhu, Z.; Su, C.; Liu, M.; Shao, Z. A Perovskite Electrocatalyst for Efficient Hydrogen Evolution Reaction. *Adv. Mater.* **2016**, *28*, 6442−6448.
(9) Papac, M.; Stevanović, V.; Zakutayev, A.; O'Hayre, R. Triple ionic−electronic conducting oxides for next-generation electrochemical devices. *Nat. Mater.* **2021**, *20*, 301−313.
(10) Peng, X.; Feng, Sh.; Lai, S.; Liu, Z.; Gao, J.; Javanbakht, M.; Gao, B. Structural engineering of rare-earth-based perovskite electrocatalysts for advanced oxygen evolution reaction. *Int. J. Hydrogen Energy* **2022**, *47*, 39470−39485.
(11) Sun, H.; Xu, X.; Chen, G.; Zhou, Y.; Lin, H.; Chen, Ch.; Ran, R.; Zhou, W.; Shao, Z. Smart Control of Composition for Double Perovskite Electrocatalysts toward Enhanced Oxygen Evolution Reaction. *ChemSusChem* **2019**, *12*, 5111−5116.
(12) Liu, Y.; Wang, Z.; Veder, J.-P. M.; Xu, Z.; Zhong, Y.; Zhou, W.; Tade, M. O.; Wang, S.; Shao, Z. Highly Defective Layered Double Perovskite Oxide for Efficient Energy Storage via Reversible Pseudocapacitive Oxygen-Anion Intercalation. *Adv. Energy Mater.* **2018**, *8*, No. 1702604.
(13) Zhang, M.; Jeerh, G.; Zou, P.; Lan, R.; Wang, M.; Wang, H.; Tao, Sh. Recent development of perovskite oxide-based electrocatalysts and their applications in low to intermediate temperature electrochemical devices. *Mater. Today* **2021**, *49*, 351−377.
(14) Choi, M.; Wang, L.; Stoerzinger, K. A.; Chung, S.; Chambers, S. A.; Du, Y. Epitaxial Design of Complex Nickelates as Electrocatalysts for the Oxygen Evolution Reaction. *Adv. Energy Mater.* **2023**, *13*, No. 2300239.
(15) Weber, M. L.; Lole, G.; Kormanyos, A.; Schwiers, A.; Heymann, L.; Speck, F. D.; Meyer, T.; Dittmann, R.; Cherevko, S.; Jooss, C.; et al.. Atomistic Insights into Activation and Degradation of $La_{0.6}Sr_{0.4}CoO_{3-\delta}$ Electrocatalysts under Oxygen Evolution Conditions. *J. Am. Chem. Soc.* **2022**, *144*, 17966−17979.
(16) Baeumer, C.; Li, J.; Lu, Q.; Liang, A. Y.; Jin, L.; Martins, H. P.; Duchoň, T.; Glöß, M.; Gericke, S. M.; Wohlgemuth, M. A.; et al. Tuning electrochemically driven surface transformation in atomically flat $LaNiO_3$ thin films for enhanced water electrolysis. *Nat. Mater.* **2021**, *20*, 674−682.
(17) Hoffmann-Urlaub, S.; Ross, U.; Hoffmann, J.; Belenchuk, A.; Shapoval, O.; Roddatis, V.; Ma, Q.; Kressdorf, B.; Moshnyaga, V.; Jooss, C. Tailoring *c* -Axis Orientation in Epitaxial Ruddlesden−Popper $Pr_{0.5}Ca_{1.5}MnO_4$ Films. *Adv. Mater. Interfaces* **2021**, *8*, No. 2002049.
(18) Watanabe, T.; Funakubo, H. Controlled crystal growth of layered-perovskite thin films as an approach to study their basic properties. *J. Appl. Phys.* **2006**, *100*, No. 051602.
(19) Angsten, T.; Martin, L. W.; Asta, M. Orientation-dependent properties of epitaxially strained perovskite oxide thin films: Insights from first-principles calculations. *Phys. Rev. B* **2017**, *95*, No. 174110.
(20) Ogimoto, Y.; Nakamura, M.; Takubo, N.; Tamaru, H.; Izumi, M.; Miyano, K. Strain-induced crossover of the metal-insulator transition in perovskite manganites. *Phys. Rev. B* **2005**, *71*, No. 060403.
(21) Abrishami, M. E.; Risch, M.; Scholz, J.; Roddatis, V.; Osterthun, N.; Jooss, C. Oxygen Evolution at Manganite Perovskite Ruddlesden-Popper Type Particles: Trends of Activity on Structure, Valence and Covalence. *Materials* **2016**, *9* (11), 921.
(22) Mierwaldt, D.; Roddatis, V.; Risch, M.; Scholz, J.; Geppert, J.; Abrishami, M. E.; Jooss, C. Environmental TEM Investigation of Electrochemical Stability of Perovskite and Ruddlesden-Popper Type Manganite Oxygen Evolution Catalysts. *Adv. Sustainable Syst.* **2017**, *1*, No. 1700109.
(23) Lole, G.; Roddatis, V.; Ross, U.; Risch, M.; Meyer, T.; Rump, L.; Geppert, J.; Wartner, G.; Blöchl, P.; Jooss, C. Dynamic observation of manganese adatom mobility at perovskite oxide catalyst interfaces with water. *Commun. Mater.* **2020**, *1*, 68.
(24) Nakamura, T.; Ling, Y.; Amezawa, K. The effect of interstitial oxygen formation on the crystal lattice deformation in layered perovskite oxides for electrochemical devices. *J. Mater. Chem. A* **2015**, *3* (3), 10471−10479.
(25) Scholz, J.; Risch, M.; Stoerzinger, K. A.; Wartner, G.; Shao-Horn, Y.; Jooss, C. Rotating Ring−Disk Electrode Study of Oxygen Evolution at a Perovskite Surface: Correlating Activity to Manganese Concentration. *J. Phys. Chem. C* **2016**, *120*, 27746−27756.
(26) Montenegro, M. J.; Lippert, T.; Müller, S.; Weidenkaff, A.; Willmott, P. R.; Wokaun, A. Pulsed laser deposition of electrochemically active perovskite films. *Appl. Surf. Sci.* **2002**, *197*, 505−511.
(27) Mierwaldt, D.; Mildner, S.; Arrigo, R.; Knop-Gericke, A.; Franke, E.; Blumenstein, A.; Hoffmann, J.; Jooss, C. In Situ XANES/XPS Investigation of Doped Manganese Perovskite Catalysts'. *Catalysts* **2014**, *4*, 129−145.
(28) Uwamino, Y.; Ishizuka, T.; Yamatera, H. X-ray photoelectron spectroscopy of rare-earth compounds. *J. Electron Spectrosc. Relat. Phenom.* **1984**, *34* (1), 67−78.
(29) Raabe, S.; Mierwaldt, D.; Ciston, J.; Uijttewaal, M.; Stein, H.; Hoffmann, J.; Zhu, Y.; Blöchl, P.; Jooss, C. In Situ Electrochemical Electron Microscopy Study of Oxygen Evolution Activity of Doped Manganite Perovskites'. *Adv. Funct Mater.* **2012**, *22*, 3378−3388.
(30) Ronge, E.; Ohms, J.; Roddatis, V.; Jones, T.; Sulzmann, F.; Knop-Gericke, A.; Schlögl, R.; Kurz, P.; Jooss, C.; Skorupska, K. Operation of calcium-birnessite water-oxidation anodes: interactions of the catalyst with phosphate buffer anions. *Sustain Energy Fuels* **2021**, *5*, 5535−5547.
(31) Duchesne, J.; Reardon, E. J. Measurement and prediction of portlandite solubility in alkali solution. *Cem. Concr. Res.* **1995**, *25*, 1043−1053.

https://doi.org/10.1021/acs.jpcc.3c06472
J. Phys. Chem. C 2024, 128, 95−103